J. Micromech. Microeng. **20** (2010) 025011 (8pp) doi:10.1088/0960-1317/20/2/025011

Three-axis micro-force sensor with sub-micro-Newton measurement uncertainty and tunable force range

S Muntwyler, F Beyeler and B J Nelson

Institute of Robotics and Intelligent Systems, ETH Zurich, Tannenstrasse 3, CH-8092 Zurich, Switzerland

E-mail: msimon@ethz.ch, fbey@ethz.ch and bnelson@ethz.ch

Received 18 September 2009, in final form 26 November 2009
Published 18 December 2009
Online at stacks.iop.org/JMM/20/025011

Abstract
The first three-axis micro-force sensor with adjustable force range from ±20 μN to ±200 μN and sub-micro-Newton measurement uncertainty is presented. The sensor design, the readout electronics, the sensor characterization and an uncertainty analysis for the force predictions are described. A novel microfabrication process based on a double silicon-on-insulator (SOI) substrate has been developed enabling a major reduction in the fabrication complexity of multi-axis sensors and actuators.

(Some figures in this article are in colour only in the electronic version)

1. Introduction

Miniature force sensors capable of measuring forces in the micro- to nano-Newton range have become a common tool in a variety of fields, such as mechanobiology, material science, microrobotics and life science. In [1, 2] the design of a single-axis capacitive force sensor and its application to study insect flight control, the mechanical characteristics of mouse embryo cells and the threshold for touch sensation in *C. elegans* [3] are shown. In [4] a sensor based on an optical, diffractive micrograting demonstrates the measurement of the injection forces into drosophila embryos and in [5] the use of an atomic force microscope (AFM), based on optical beam deflection, shows the measurement of molecular interaction forces. A sensor based on the trapping of a magnetic particle in a magnetic field is shown in [6] and is used to measure the force-extension curves of DNA molecules. More recently many of these principles have been employed to develop multi-axis sensors. For many applications additional force components offer a great advantage, e.g. in the case of automated cell injection [7] since a misalignment of the cell and the injection pipette can be detected and compensated. In [8, 9] two three-axis force sensors based on piezoresistive materials are presented and used for the manipulation of embryo cells. A three-axis capacitive force/torque sensor for the measurement of forces and torque acting on a magnetic microrobot has been developed in [10], and in [11] a six-axis force/torque sensor is described.

All these sensors are designed for a specific force range and must be redesigned when used in different applications. It is desirable to have a sensor with an adjustable range to ensure its optimal characteristics for a large variety of applications. Additionally, to date little work has been published on the calibration of multi-axis micro-force sensors and their uncertainty analysis. The results obtained from a sensor are complete only when accompanied by a statement of uncertainty indicating their quality. This paper presents the design, optimization, fabrication and characterization of the first microfabricated three-axis force sensor with sub-micro-Newton measurement uncertainty. The force range of the sensor can be electronically tuned while taking measurements. The sensor calibration and the most important sensor characteristics and their influence on the measurement uncertainty are presented. Finally, the novel microfabrication process is described enabling a major reduction in the fabrication complexity of multi-axis sensors and actuators.

2. Working principle

This work focuses on capacitive force sensing because of its low sensitivity to changes in environmental conditions such

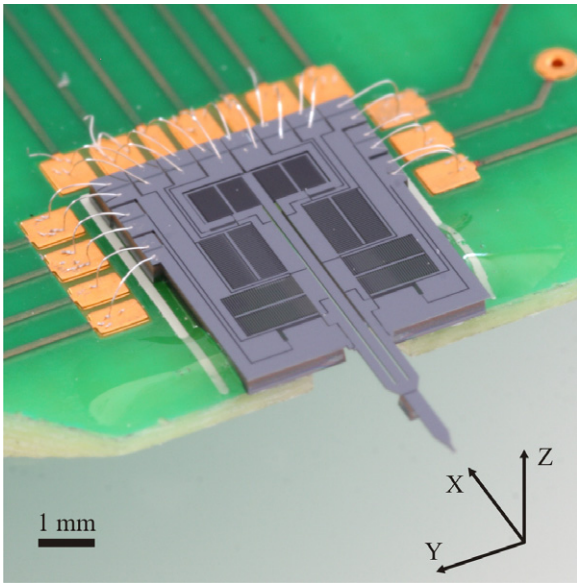

Figure 1. The MEMS-based capacitive three-axis tunable micro-force sensor. The sensor dimensions without the sensor probe are 5 mm by 6 mm and the probe length is 3 mm.

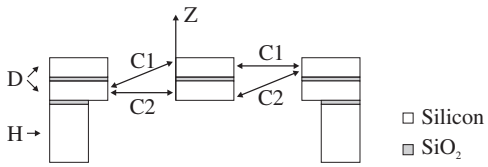

Figure 2. Cross-section of the sensing capacitor visualizing the out-of-plane sensing principle.

as light, temperature and humidity, its stable output signal (low sensor drift) and its compact size, compared to an optical beam AFM. Figure 1 shows the sensor. It consists of a movable body with a 3 mm long probe suspended by flexures within an outer frame. A force applied to the probe results in a relative motion of the body and the frame, which can be measured by capacitive electrodes as a change of capacitance. By allowing the sensor to move in multiple directions and by using several of these capacitive displacement sensors, forces in multiple axes can be measured. The capacitive electrodes are arranged as parallel plate capacitors, enabling them to measure displacements in two configurations: transversely, through a change in the gap width between the capacitor plates and laterally, through a change in the overlapping area of the capacitor plates. The transverse way offers very high sensitivity but a lack of linearity, which can be overcome by differentially measuring two capacitive changes in opposite directions. The sensor output is then proportional to the difference in capacitance. More details about capacitive sensing can be found in [12]. Forces in the sensor plane (x and y) are measured transversely with two capacitor pairs. However, due to the planar MEMS-based fabrication, forces or displacements out of the sensor plane (z-direction) need to be measured laterally. Figure 2 shows a cross-section of the z-axis sensing capacitor configuration. The sensor is fabricated based on a double silicon-on-insulator (SOI) substrate. The

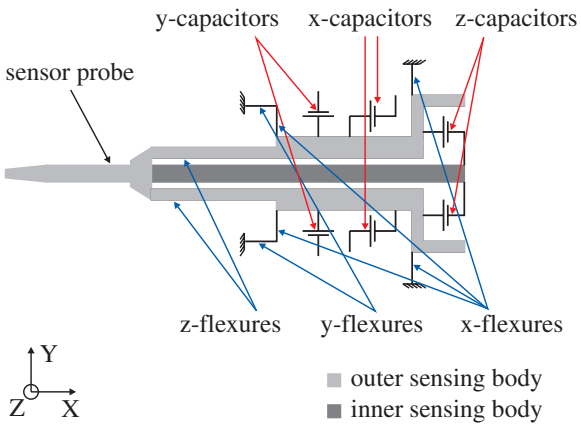

Figure 3. Sensor schematic (non-movable, outer frame not shown).

relatively thick silicon handle layer (H) forms the outer frame of the sensor, whereas the two thin silicon device layers (D) form the active element and the movable body. All the layers are electrically isolated by a silicon dioxide (SiO_2) layer. A single device layer would be sufficient to measure displacements in three directions, but the additional layer enables the distinction between positive and negative forces. In this case the differential capacitance $C1$–$C2$ is negative when the inner sensing body moves up ($z > 0$) and positive when it moves down ($z < 0$).

In figure 3, the schematic of the sensor is shown. Due to the unequal sensitivity of transversal in-plane sensing compared to lateral out-of-plane sensing, these degrees of freedom are divided into two sensing bodies suspended within each other. The outer body measures displacements in x and y (and, therefore, forces relative to them) and the inner sensing body displacements (forces) relative to the outer sensing body in z.

3. Sensor design

The sensor is designed to measure forces of up to 200 μN in x, y and z. Multiple sensor configurations (position and geometry of flexures, capacitors and movable bodies) have been analytically compared. Besides the sensitivity criterion for each axis, the most important factor in the multi-axis sensor design is the decomposability of the force components. To ensure a minimum cross-coupling between the different axes, each capacitor pair is dedicated to a single force component and placed such that the main contribution to an output signal can be directly related to the force in the corresponding direction. Therefore, the x-capacitor is mainly sensitive to forces in x, the y-capacitor to forces in y and the z-capacitor to forces in z. Similar considerations have been made for the flexures, such that by changing the dimensions of the flexures the mechanical stiffness of the sensor can be independently adjusted for each axis.

Figure 4 shows the mechanical response of the sensor to each force component. A force applied in x will result in a parallel movement of the sensing bodies and, therefore, produces only a change in the x-capacitance. Since always

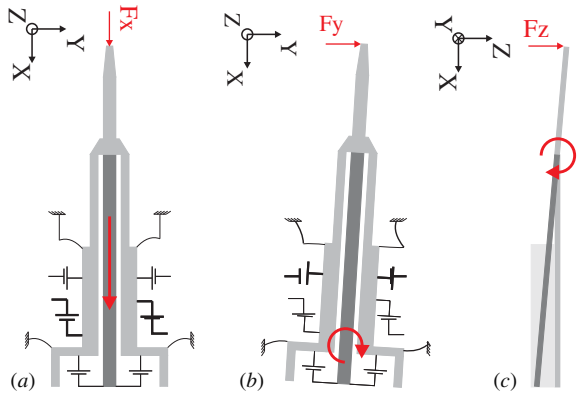

Figure 4. Sensor schematic and the mechanical response of applied forces.

one of the parallel plate capacitor electrodes is longer than the other, a parallel relative movement (as the case for the *y*-capacitor) will not result in a change of the overlapping area and thus not affect there capacitance, as shown in figure 4(*a*).

Forces in *y* result in a rotation of the sensing bodies. To ensure high sensitivity to these rotations, the *y*-capacitor pair is placed as far from the point of rotation as possible, as shown in figure 4(*b*). The absolute capacitances in the *x*-capacitors will both change with the same sign due to a force in *y*, resulting in no change in the differential capacitance.

Due to the lower sensitivity of lateral sensing, forces in *z* need to produce a much larger deflection of the capacitor electrodes than forces in *x* or *y*. Therefore, an amplification lever is integrated, as shown in figure 4(*c*), and the *z*-capacitor is placed as far from the sensor tip as possible to maximize its leverage effect. Using this method, the *z*-flexure stiffness does not need to be significantly reduced. Additionally, forces in *z* will only result in a signal in the *z*-capacitors for two reasons. Firstly, the relative motion of the outer sensing body to the base will equally affect the two capacitors in a pair and, therefore, not change the differential capacitance. Secondly, due to the aspect ratio of the flexures in *x* and *y* (much thicker than wide), the out-of-plane motion can be neglected.

An ANSYS finite element model (FEM) has been created to calculate the quantitative mechanical response of the sensor to an applied force at its probe. This enables the optimization of the flexure geometry for a certain target sensitivity along the three axes. The deflections at the position of each capacitor and the corresponding differential signal change were used as the design criteria and the flexure dimensions as the design parameter. Starting with an initial estimate of the flexure dimensions the FEM model was used in an optimization loop to determine the difference from the target deformations in each capacitor and for each force direction. By scaling the flexure dimensions with these errors, the ideal flexure geometry could be found, not only ensuring the desired signal change at the target force in the corresponding capacitor pair, but also minimizing the signals in all the other capacitor pairs. The resulting flexures are shown in figure 5 and their dimensions in table 1. Since all the capacitors need to have electrical contact

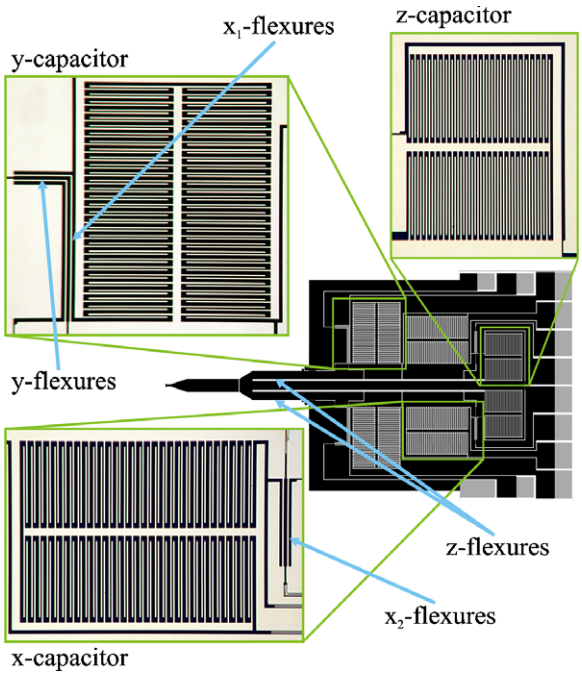

Figure 5. Close-up views of the micro-force sensor. All the capacitors have a plate length of 500 μm and a gap width of 7 μm and 20 μm respectively.

Table 1. Flexure dimensions.

	Width (μm) A/B	Length (μm) A	Length (μm) B
x_1-flexure	10	835	865
x_2-flexure	10	537	537
y-flexure	10	314	344
z-flexure	183	1900	1900

to the outer frame, two flexures (A and B) at each point had to be fabricated instead of one to produce the required electrical connections.

4. Fabrication

The force sensors are fabricated by a MEMS-based bulk silicon microfabrication process. In [10] a three-mask process based on an SOI substrate describes the fabrication of sensors measuring deflections in the sensor plane. In [11] a more complex five-mask fabrication process including wafer bonding is presented, enabling the measurement of in- and out-of-plane displacements.

In this work a three-mask process has been developed, similar in complexity to the SOI process published in [10], but enabling three-axis sensors or actuators. It is based on a double SOI substrate with sequential etching of the two device layers by dry etching. Wafer bonding is not required. Even though commercially available double SOI substrates are more expensive, the reduction of photomasks and fabrication steps results in a higher yield rate and, therefore, in a more economical fabrication. In figure 6 the fabrication process is depicted. The photoresist layers are shown only in the steps

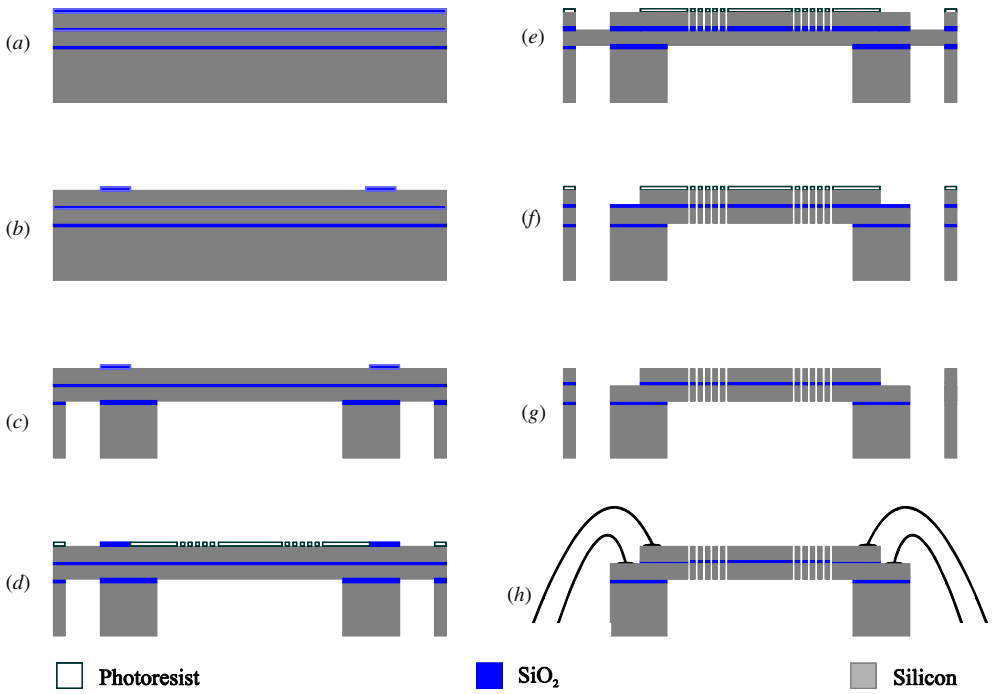

Figure 6. Microfabrication process. (*a*) A 100 mm diameter double SOI wafer is used as a substrate, with a handle layer thickness of 400 μm, two device layers with a thickness of 25 μm and three SiO_2 layers with a thickness of 2 μm. All silicon layers have a $\langle 1\,0\,0 \rangle$ orientation and are highly *p*-doped. (*b*) The SiO_2 on the top device layer is structured with reactive ion etching (RIE) to form an etch mask in the regions, where in the last step, wires are bonded to the lower device layer. (*c*) The handle layer is etched by deep reactive ion etching (DRIE) where the SiO_2 acts as an etch stop and is removed subsequently by RIE. This will form the outer frame of the sensors. Since the sensor features a probe overhanging the rest of the device, dicing cannot be done to separate the individual dies. Therefore, a cavity surrounding the sensor is etched in this step. (*d*) The photoresist (AZ 4562) is applied with a thickness of 5 μm and structured to form a second etch mask on the top device layer. This defines the active parts of the sensor such as comb drives, flexures and the movable bodies. (*e*) The wafer is mounted onto a support wafer using heat-conductive grease (cool grease, AI Technology), and the top device layer is etched by DRIE. Subsequently the underlying SiO_2 is etched by RIE. The SiO_2 etch mask, formed in A, is removed during this step as well. (*f*) The lower silicon device layer is structured by DRIE with the same photoresist mask completely releasing the devices. At the same time the top device layer is etched in the regions where the SiO_2 mask was removed in step E. (*g*) The SiO_2 on the lower bonding regions is removed by RIE and the remaining photoresist stripped in oxygen plasma. (*h*) In the last step the sensors are glued onto a circuit board and wire bonded.

involved in the sequential etching of the two device layers (*d*)–(*f*).

5. Readout electronics

The electronic readout of the sensing capacitance is based on the impedance relation measurement where two periodic, 180° phase-shifted excitation voltages are applied to a capacitor pair. The demodulated response of the common electrode is then proportional to the ratio of the two capacities [10]. A commercial capacitance-to-voltage converter IC (CVC 1.1, GEMAC) is used to interface each capacitor pair (C1 and C2) on the sensor. This mixed signal-integrated circuit consists of a charge integrator with integration capacitance C_{int}, a sample hold cell, a second-order low-pass filter where the cut-off frequency has been set to 5 kHz and an amplifier stage with an additional gain that can be set by a serial interface. The analog part of the block diagram of the readout is shown in figure 7. Since the sensor is designed to measure positive and negative forces, all the internal operational amplifiers and the output voltage are trimmed to the midpoint of their range of 0–4 V, so forces will result in maximum voltage changes of ±2 V. All the settings are stored in an integrated EEPROM

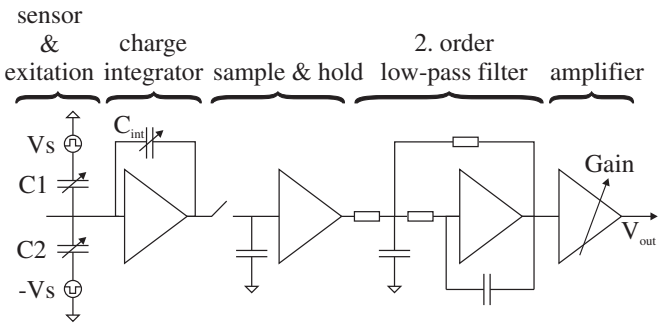

Figure 7. Block diagram of the capacitance-to-voltage converter IC (CVC 1.1).

cell. The serial interface and the analog voltage readout have been realized using Labview and a data acquisition card (NI PCI-6259). By changing the values of C_{int} and gain, shown in (1), the sensitivity of the sensor can be electronically tuned to the appropriate force range of the specific application:

$$V_{\text{out}} \propto \text{Gain} \cdot \frac{C1 - C2}{C_{\text{int}}}. \qquad (1)$$

6. Sensor characterization

6.1. Calibration

The most commonly used micro-force sensor, the AFM, has led to the development of a large number of methods to calibrate forces in the micro- and nano-Newton range [13]. However, the accuracy of these methods is unknown since none of them are traceable to the Système International (SI) d'unités. The unit force is derived from the definition of Newton using a combination of base SI units (kg, m and s) [14].

Increasing effort is being made in multiple national measurement institutes (NMI) to create an SI traceable reference standard for the calibration of small forces. An overview of the different approaches can be found in [14]. However, when calibrating samples pre-calibrated by another NMI, even NMI's show differences of up to 30% in the results [15]. Currently there is no commercial, SI traceable reference force sensor system in the micro- and nano-Newton range available. Therefore, in this work, no claim is made of absolute accuracy in the calibration performed. For the calibration, as a comparison of the sensor with another standard, a commercially available, calibrated micro-force sensor (FT-S540, Femtotools) is used as a reference, and the uncertainty analysis is carried out relative to this.

There are no standards or norms for the calibration of multi-axis force sensors and the calculation of their accuracy, as they exist in the single-axis case (DIN EN ISO 376) [16]. There are some methods published for the calibration of multi-axis forces sensors, e.g. using the shape from motion technique [17], but they are based on mathematical models and, therefore, their accuracy cannot be determined. In this work the sensor is calibrated by subsequently applying a reference force in all directions (x, y and z) using a reference force sensor:

$$\mathbf{F} = \mathbf{V} \cdot \mathbf{A}. \tag{2}$$

The goal is to obtain the calibration matrix $\mathbf{A}^{3\times 3}$, which describes the relationship between the output voltages $\mathbf{V} = [V_x\, V_y\, V_z]$ of the sensor and the applied forces $\mathbf{F} = [F_x\, F_y\, F_z]$:

$$\mathbf{V}_c = \begin{bmatrix} V_{x_1} & \cdots & V_{x_n} & V_{x_1} & \cdots & V_{x_h} & V_{x_1} & \cdots & V_{x_k} \\ V_{y_1} & \cdots & V_{y_n} & V_{y_1} & \cdots & V_{y_h} & V_{y_1} & \cdots & V_{y_k} \\ V_{z_1} & \cdots & V_{z_n} & V_{z_1} & \cdots & V_{z_h} & V_{z_1} & \cdots & V_{z_k} \end{bmatrix}^T \tag{3}$$

$$\mathbf{F}_c = \begin{bmatrix} F_{x_1} & \cdots & F_{x_n} & 0_1 & \cdots & 0_h & 0_1 & \cdots & 0_k \\ 0_1 & \cdots & 0_n & F_{y_1} & \cdots & F_{y_h} & 0_1 & \cdots & 0_k \\ 0_1 & \cdots & 0_n & 0_1 & \cdots & 0_h & F_{z_1} & \cdots & F_{z_k} \end{bmatrix}^T. \tag{4}$$

As mentioned in section 3, the mechanical stiffness is different in each axis. Therefore, the number of calibration data points will be different in each direction. Before solving the system of equations, the raw calibration force and voltage data (3, 4) are linearly interpolated ($F_{\mathrm{c,ipol}}$, $V_{\mathrm{c,ipol}}$) thereby weighting each axis equally. Using the least-squares method (6) and minimizing the residual **r,** the best estimate of the calibration matrix $\widehat{\mathbf{A}}$ is found. To facilitate the understanding of the uncertainty analysis, shown in the next section, the system of equations is divided into three systems. (The results of the calibration are shown in section 6.3.)

$$\mathbf{F}_{\mathrm{c,ipol}} = \mathbf{V}_{\mathrm{c,ipol}} \cdot \widehat{\mathbf{A}} + \mathbf{r}_{\min} \tag{5}$$

$$\widehat{\mathbf{A}}_j = \left(\mathbf{V}^T_{\mathrm{c,ipol}} \cdot \mathbf{V}_{\mathrm{c,ipol}}\right)^{-1} \cdot \mathbf{V}^T_{\mathrm{c,ipol}} \cdot \mathbf{F}_{j,\mathrm{c,ipol}} \quad \text{with} \quad j = x,y,z \tag{6}$$

$$\widehat{\mathbf{A}} = [\widehat{\mathbf{A}}_x \quad \widehat{\mathbf{A}}_y \quad \widehat{\mathbf{A}}_z]. \tag{7}$$

6.2. Sensor characteristics and measurement uncertainties

The result of a measurement is only an approximation of the value of the measurand and, thus, is complete only when accompanied by a statement of the uncertainty of that estimate [18]. The measurement uncertainty is a parameter associated with the results of a measurement that characterizes the dispersions of the values that could reasonably be attributed to the measurand [19]. Therefore, besides the calibration matrix and the corresponding sensing range, the most important characteristics of the sensor are measured and their influence on the measurement uncertainty calculated.

- *Force range*. The maximum measurable force can be found by multiplying the calibration matrix with the maximum voltage change in all axes (±2 V).
- *Resolution*. The smallest force increment that can be detected, limited by the noise in the sensor output. The uncertainty in the force measurement due to noise is given by the standard deviation of the output voltages multiplied by the calibration matrix.
- *Sensor drift*. The change in the output signal without any change of the applied force over a certain time period. The uncertainty due to drift is calculated using (8), the root mean square of the voltage change $\mathbf{\Delta V}$ in the time period t (10 s), where n is the number of intervals measured over:

$$u_{\mathrm{drift},j}(t) = \sqrt{\frac{\sum \Delta \mathbf{V}(t)^2}{n-1}} \cdot \widehat{\mathbf{A}}_j. \tag{8}$$

- *Cross sensitivity.* Sensitivity of a sensor output to a force applied in another direction. This characteristic is related to how good the sensor can separate the different force components from each other.
- *Nonlinearity.* The calibration matrix is a linear representation of the sensor. A nonlinearity in the sensor's characteristics can result in a measurement error and, therefore, to an increased uncertainty in the results.
- *Uncertainties in the calibration matrix.* All sources of uncertainties related to the calibration matrix, such as the cross-sensitivity and nonlinearity, are combined. The uncertainty in a force prediction shown in (9) can be calculated using the covariance matrix in (10) and the mean square error ${\delta_j}^2$ in (11), where $n+h+k$ is the number of calibration data points. For these calculations the raw calibration data V_c, F_c are used. The diagonal elements in each of the covariance matrices are the variances of the components in the calibration matrix:

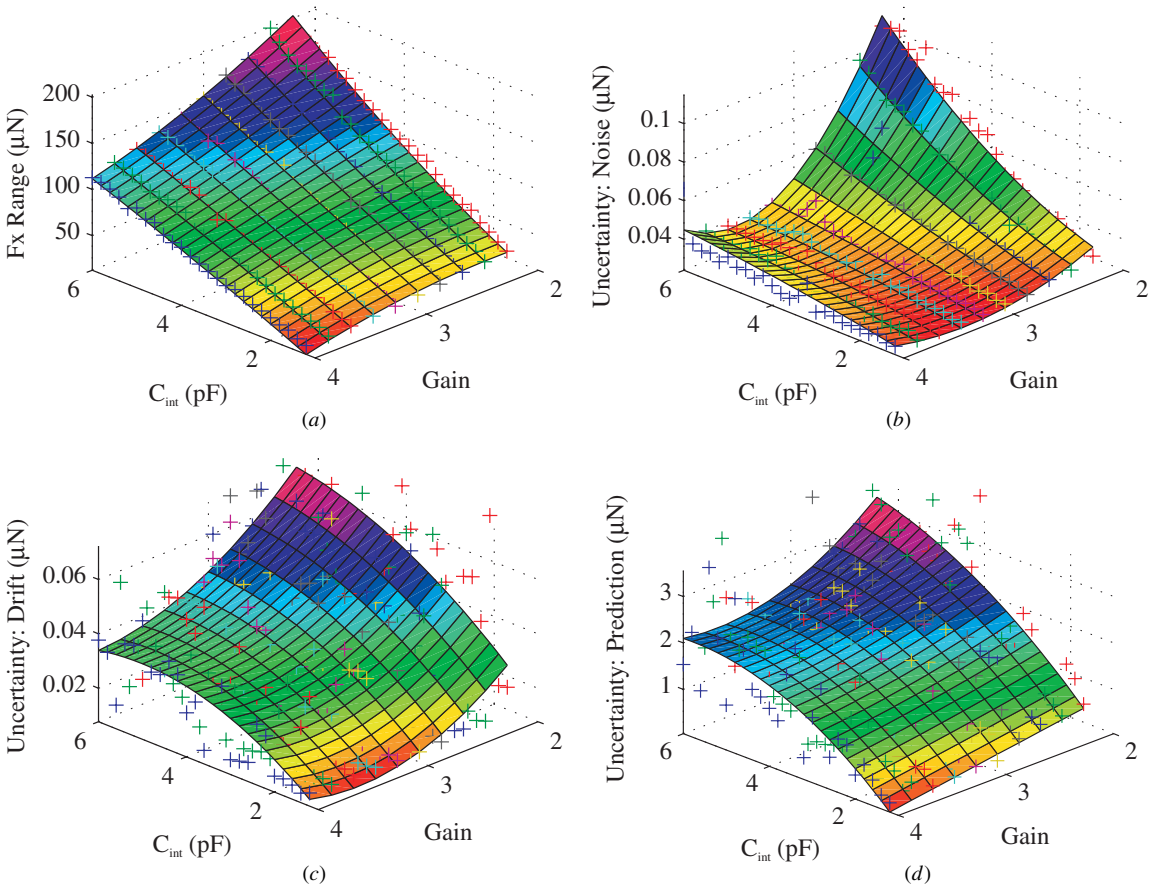

Figure 8. (*a*) Force range F_x as a function of C_{int} and gain. (*b*) Uncertainty in F_x due to noise in function of C_{int} and gain. (*c*) Uncertainty in F_x due to sensor drift over 10 s in function of C_{int} and gain. (*d*) Maximum uncertainty in F_x prediction in function of C_{int} and gain.

$$u_{\text{Prediction},j} = \sqrt{\delta_j^2 + \mathbf{V}_p \cdot \text{Var}(\widehat{\mathbf{A}}_j) \cdot \mathbf{V}_p^T} \tag{9}$$

$$\text{Var}(\widehat{\mathbf{A}}_j) = \delta_j^2 \cdot \left(\mathbf{V}_c^T \mathbf{V}_c\right)^{-1} \tag{10}$$

$$\delta_j^2 = \frac{(\mathbf{F}_{jc} - \widehat{\mathbf{F}}_j)^T (\mathbf{F}_{jc} - \widehat{\mathbf{F}}_j)}{n + h + k - 3} \qquad \text{with} \quad \widehat{\mathbf{F}}_j = \mathbf{V}_c \cdot \widehat{\mathbf{A}}_j. \tag{11}$$

- *Expanded combined uncertainty.* By combining all the sources of measurement uncertainty together and multiplying them with the coverage factor k, the expanded combined uncertainty can be calculated as shown in (12). Utilizing the central limit theorem a normal distribution is assumed, and, therefore, a coverage factor of 1 or 2 will result in a confidence level of approximately 68% or 95%, respectively.

$$u_j = k \cdot \sqrt{u_{j,\text{Drift}}^2 + u_{j,\text{Noise}}^2 + u_{j,\text{Predictiion}}^2}. \tag{12}$$

- *Resonate frequency.* The bandwidth of the sensor is limited by the lowest resonant frequency of 1570 Hz, measured using a laser Doppler vibrometer and validated using FEM modeling.

6.3. Sensor tuning and the corresponding characteristics

Depending on the application, a specific force range is required. By tuning the range of the sensor, the ideal sensor characteristics and the smallest possible measurement uncertainties can be guaranteed. Therefore, the sensor is characterized for a number of different settings of the readout electronics. The integrator capacitance C_{int} has been varied from 1.2 pF to 6.0 pF in 0.2 pF steps and the amplifier gain from 2.2 to 4.0 in 0.2 steps. For each combination of these two parameters the sensor has been calibrated five times along each axis, the sensor characteristics have been recorded and the corresponding measurement uncertainties calculated. The resulting data sets for x, from a total of 3750 calibrations, can be seen in figure 8. The raw characterization data are shown as +, whereas the surface plots show a fit using a second-order polynomial in two variables, fitted using a least-squares algorithm.

Using this setting range the force range of the sensor can be changed from approximately ± 20 μN to ± 200 μN. The calibration curves for the minimum and maximum sensor range are shown in figure 9. The arrows between the main components, which correlate with the diagonal elements in the calibration matrix, indicate the range in which the calibration curves can be adjusted. The corresponding uncertainty components are shown in table 2. The non-diagonal entries in the calibration matrix are approximately zero, which can be verified in the calibration plots. This is an indication that the goal, to mechanically decompose the forces, has been successfully realized. Depending on the application and

Table 2. Sensor characteristics at two different electronic settings.

Gain	4	3
C_{int} (pF)	1.2	2.2
A (μN V^{-1})	$\begin{bmatrix} 10.80 & 0.39 & -2.12 \\ 0.24 & 9.89 & 0.80 \\ -0.04 & -0.24 & 18.44 \end{bmatrix}$	$\begin{bmatrix} 95.61 & -0.42 & -0.20 \\ -1.11 & 83.43 & -3.50 \\ -2.12 & -0.02 & 109.18 \end{bmatrix}$
Sensing range (μN)		
F_x	±22	±192
F_y	±20	±176
F_z	±31	±222
Mechanical resonant frequency (lowest)	1570 Hz	
Uncertainty: noise measured at 10 Hz readout frequency (μN)		
x	0.03	0.11
y	0.03	0.07
z	0.05	0.12
Uncertainty: drift over 10 s (μN)		
x	0.01	0.04
y	0.01	0.04
z	0.02	0.07
Uncertainty: prediction (μN)		
x	0.17–0.20	4.46–4.51
y	0.23–0.26	4.69–4.75
z	0.09–0.10	2.54–2.57

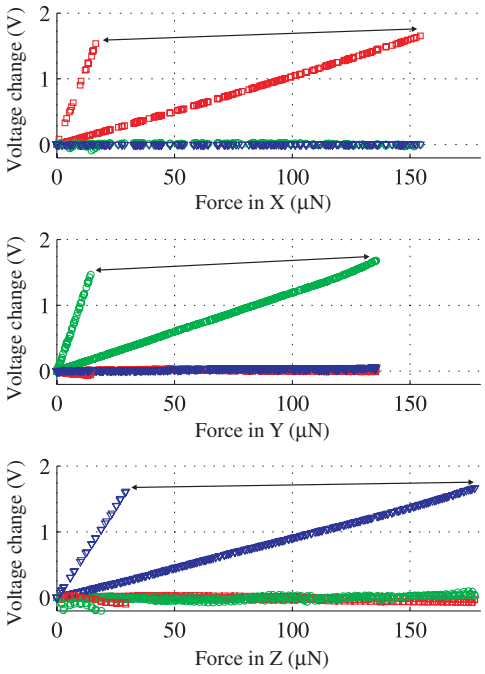

Figure 9. The calibration plots of the force sensor for two different readout settings. Squares indicate the raw calibration data V_x, circles V_y and triangles V_z.

the range of forces needed to be measured, the sensor can now be electronically tuned during the measurements to the appropriate sensor range, since it has been characterized for all the settings in advance.

The main contribution in the uncertainty components, shown in table 2, comes from the uncertainty in the force prediction. The upper level in these intervals corresponds to the uncertainty at the maximum output voltage of the sensor and the lower limit to the minimum which is proportional to the root mean square of the difference between the calibration data and the force prediction. Therefore, fluctuations and nonlinearities in the calibration curves, as seen in figure 9, have a major influence in the calculation of the measurement uncertainty. These fluctuations are artifacts of the calibration method and demonstrate the major challenge of applying reference force vectors at exact locations and orientations without damaging the fragile sensor structures.

7. Conclusion

An electronically tunable three-axis micro-force sensor, its design, fabrication and characterization have been presented. It has been designed such that the cross-sensitivities and additional uncertainties related to cross-sensitivity are reduced. The designed sensor enables force measurements in a range between ±20 μN and ±200 μN with a resolution down to 30 nN. Due to the unavailability of a commercial, SI traceable reference force sensor in the micro- and nano-Newton range, the measurement uncertainties have been evaluated relative to a reference force sensor in the 0.1 μN range at the highest resolution. The main contributions of this work are as follows.

- The first three-axis micro-force sensor enabling force measurements of sub-micro-Newton.
- A tunable force range, enabling the sensor to be optimized for an application while measuring.

- A novel three-mask fabrication process enabling the fabrication of three-axis transducers with a major reduction in fabrication complexity.

Acknowledgment

This work is conducted with financial support from the project 'Hybrid Ultra Precision Manufacturing Process Based on Positional and Self-Assembly for Complex Micro-Products (HYDROMEL)' funded by the European Commission under the 6th Framework Program (FP6).

References

[1] Sun Y and Nelson B J 2007 MEMS capacitive force sensors for cellular and flight biomechanics *Biomed. Mater.* **2** S16-22

[2] Graetzel C F, Fry S N, Beyeler F, Sun Y and Nelsons B J 2008 Real-time microforce sensors and high speed vision system for insect flight control analysis *Spr. Tra. Adv. Robot.* **39** 451–60

[3] Doll J C, Muntwyler S, Beyeler F, Geffeney S, Goodman M B, Nelson B J and Pruitt B L 2009 Measuring thresholds for touch sensation in *C. elegans Proc. in the 5th Int. Conf. on Microtechnologies in Medicine and Biology (MMB) (Québec)*

[4] Zhang X J, Zappe S, Bernstein R W, Sahin O, Chen C C, Fish M, Scott M and Solgaard O 2003 Integrated optical diffractive micrograting-based injection force sensor *Transducers '03: Digest of Technical Papers (Boston)* vols 1 and 2 1051–4

[5] Hugel T and Seitz M 2001 The study of molecular interactions by AFM force spectroscopy *Macromol. Rapid Commun.* **22** 989–1016

[6] Gosse C and Croquette V 2002 Magnetic tweezers: micromanipulation and force measurement at the molecular level *Biophys. J.* **82** 3314–29

[7] Sun Y, Nelson B J, Potasek D P and Enikov E 2002 A bulk microfabricated multi-axis capacitive cellular force sensor using transverse comb drives *J. Micromech. Microeng.* **12** 832–40

[8] Sieber A, Valdastri P, Houston K, Eder C, Tonet O, Menciassi A and Dario P 2008 A novel haptic platform for real time bilateral biomanipulation with a MEMS sensor for triaxial force feedback *Sensors Actuators* A **142** 19–27

[9] Tibrewala A, Phataralaoha A and Buttgenbach S 2008 Simulation, fabrication and characterization of a 3D piezoresistive force sensor *Sensors Actuators* A **147** 430–5

[10] Beyeler F, Muntwyler S, Nagy Z, Graetzel C, Moser M and Nelson B J 2008 Design and calibration of a MEMS sensor for measuring the force and torque acting on a magnetic microrobot *J. Micromech. Microeng.* **18** 025004

[11] Beyeler F, Muntwyler S and Nelson B J 2009 A six-axis MEMS force-torque sensor with micro-Newton and nano-Newtonmeter resolution *J. Microelectromech. Syst.* **18** 433–41

[12] Sun Y, Fry S N, Potasek D P, Bell D J and Nelson B J 2005 Characterizing fruit fly flight behavior using a microforce sensor with a new comb-drive configuration *J. Microelectromech. Syst.* **14** 4–11

[13] Burnham N A, Chen X, Hodges C S, Matei G A, Thoreson E J, Roberts C J, Davies M C and Tendler S J B 2003 Comparison of calibration methods for atomic-force microscopy cantilevers *Nanotechnology* **14** 1–6

[14] Pratt J R, Kramar J A, Newell D B and Smith D T 2005 Review of SI traceable force metrology for instrumented indentation and atomic force microscopy *Meas. Sci. Technol.* **16** 2129–37

[15] Gates R S and Pratt J R 2006 Prototype cantilevers for SI-traceable nano-Newton force calibration *Meas. Sci. Technol.* **17** 2852–60

[16] 2004 *BS EN ISO 376 Metallic Materials—Calibration of Force-Proving Instruments Used for the Verification of Uniaxial Testing Machines* (Geneva: International Organisation of Standardization)

[17] Kim K, Sun Y, Voyles R M and Nelson B J 2007 Calibration of multi-axis MEMS force sensors using the shape-from-motion method *IEEE Sensors J.* **7** 344–51

[18] 1993 *Guide to the Expression of Uncertainty in Measurement* (Geneva: International Organisation of Standardization)

[19] 1993 *International Vocabulary of Basic and General Terms in Metrology* (Geneva: International Organisation of Standardization)